Low-dose CT for the spatial normalization of PET images: A validation procedure for amyloid-PET semi-quantification

Luca Presotto[a], Leonardo Iaccarino[b,c], Arianna Sala[b,c], Emilia G. Vanoli[a], Cristina Muscio[d], Anna Nigri[d], Maria Grazia Bruzzone[d], Fabrizio Tagliavini[d], Luigi Gianolli[a], Daniela Perani[a,b,c,*], Valentino Bettinardi[a]

[a] Nuclear Medicine Unit, IRCCS San Raffaele Hospital, Milan, Italy
[b] Vita-Salute San Raffaele University, Milan, Italy
[c] In vivo human molecular and structural neuroimaging Unit, Division of Neuroscience, IRCCS San Raffaele Scientific Institute, Milan, Italy
[d] Fondazione Istituto di Ricovero e Cura a Carattere Scientifico Istituto Neurologico Carlo Besta, Milano, Italy

A B S T R A C T

The reference standard for spatial normalization of brain positron emission tomography (PET) images involves structural Magnetic Resonance Imaging (MRI) data. However, the lack of such structural information is fairly common in clinical settings. This might lead to lack of proper image quantification and to evaluation based only on visual ratings, which does not allow research studies or clinical trials based on quantification.

PET/CT systems are widely available and CT normalization procedures need to be explored. Here we describe and validate a procedure for the spatial normalization of PET images based on the low-dose Computed Tomography (CT) images contextually acquired for attenuation correction in PET/CT systems. We included $N = 34$ subjects, spanning from cognitively normal to mild cognitive impairment and dementia, who underwent amyloid-PET/CT (^{18}F-Florbetaben) and structural MRI scans. The proposed pipeline is based on the SPM12 unified segmentation algorithm applied to low-dose CT images. The validation of the normalization pipeline focused on 1) statistical comparisons between regional and global ^{18}F-Florbetaben-PET/CT standardized uptake value ratios (SUVrs) estimated from both CT-based and MRI-based normalized PET images (SUVr$_{CT}$, SUVr$_{MRI}$) and 2) estimation of the degrees of overlap between warped gray matter (GM) segmented maps derived from CT- and MRI-based spatial transformations.

We found negligible deviations between regional and global SUVrs in the two CT and MRI-based methods. SUVr$_{CT}$ and SUVr$_{MRI}$ global uptake scores showed negligible differences (mean $\pm$ sd 0.01 $\pm$ 0.03). Notably, the CT- and MRI-based warped GM maps showed excellent overlap (90% within 1 mm).

The proposed analysis pipeline, based on low-dose CT images, allows accurate spatial normalization and subsequent PET image quantification. A CT-based analytical pipeline could benefit both research and clinical practice, allowing the recruitment of larger samples and favoring clinical routine analysis.

1. Introduction

The evaluation of biomarkers for the early diagnosis of neurodegenerative conditions causing dementia has been increasingly recognized as of outmost importance in research and clinical practice (Ahmed et al., 2014; Albert et al., 2011; Armstrong et al., 2013; Dubois et al., 2014; Iaccarino et al., 2017; McKeith et al., 2017; McKhann et al., 2011a; Rascovsky et al., 2011; Sperling et al., 2011). As for Alzheimer's Disease (AD), the development of Positron Emission Tomography (PET) techniques to investigate brain amyloid accumulation (amyloid-PET)

brought landmark changes in clinical neuroscience research (Villemagne, 2016). The reliability of PET tracers for in vivo amyloid assessment is supported by their correlation with post-mortem amyloid plaque measurement (Clark et al., 2012; Sabri et al., 2015; Wolk, 2011).

To date, their mandatory adoption in clinical trials and the great potential for diagnostic purposes is recognized, in particular to rule out AD pathology (Vandenberghe et al., 2013b; Vandenberghe et al., 2013a). Amyloid PET imaging plays a fundamental role for the inclusion and exclusion of subjects in clinical trials based on anti-amyloid treatments (Sperling et al., 2014a, 2014b), and it has been used as an

outcome measure as well (Salloway et al., 2014; Sevigny et al., 2016). The positivity of an amyloid-PET scan is commonly assessed qualitatively through a visual evaluation of the PET radiotracer distribution, in accordance to tracer-specific guidelines (Rowe and Villemagne, 2013).

A correct and reliable quantification of regional amyloid burden with PET, however, is considered mandatory to avoid the limitations of the operator-dependent visual classification, especially in longitudinal studies (Perani et al., 2014a,b). The most commonly adopted semi-quantification techniques involve tracer-specific approaches to estimate regional amyloid burden based on Standardized Uptake Value Ratio (SUVr) measurements. SUVrs are obtained by comparing tracer uptake in target regions to a reference area devoid of specific uptake. By comparing SUVrs in AD patients with SUVrs obtained in healthy volunteers, previous studies derived cut-off thresholds that could discriminate between amyloid positive and amyloid negative individuals (Barthel et al., 2011; Chiotis et al., 2015; Fleisher, 2011; Nordberg et al., 2013; Oh et al., 2015; Ong et al., 2015; Vandenberghe et al., 2010). Semi-quantitative amyloid burden is generally estimated on average (composite) SUVr based on neocortical regions, usually including frontal, parietal, temporal and cingulate regions (Clark et al., 2012; Fleisher, 2011). The adopted reference regions for amyloid PET SUVr can vary and may include the whole cerebellum, the cerebellar gray matter (GM) and/or specific portions of the white matter (WM) (Brendel et al., 2015; Schmidt et al., 2015). Of note, the implementation of semi-quantification techniques can also introduce variability, especially with respect to differences in analysis procedures and scan protocols. All these factors can heavily impact the classification of amyloid burden, with considerable effects in research studies and consequences in clinical trials (e.g. inclusion/exclusion of subjects). Among the most important factors there are: i) the selection of regions of interest (ROIs); ii) the selection of reference regions and iii) the choice of running quantifications in either native or standard space, with the latter being strongly influenced by the spatial normalization algorithms.

In an ideal setting, structural Magnetic Resonance Imaging (MRI) scans are available for each subject, allowing high precision spatial normalization and ROIs definition. Conveying the PET images to standard space can offer the use of standardized, published atlases with regions of interest, such as Automatic Anatomical Labeling: AAL (Tzourio-Mazoyer et al., 2002), Talairach Daemon: TD (Lancaster et al., 2000; Lancaster et al., 1997), Individual Brain Atlas: IBA (Aleman-Gomez et al., 2006), allowing for the definition of ROIs and to estimate regional SUVrs. In a routine diagnostic setting, however, MRI data are not always available, thus preventing an MRI-based spatial normalization of the amyloid-PET images to a standard space. For many centers, the lack of an MRI-based normalization pipeline prevents any further quantification.

To overcome this limitation, several PET-only pipelines for spatial normalization have been developed, based on custom or simulated PET templates (Hutton et al., 2015; Lundqvist et al., 2013; Saint-Aubert et al., 2014). These templates enable an accurate PET image warping and semi-quantification, but they are tracer-specific, limiting their utilization to radioligands with similar radioactivity distributions. Furthermore, to perform an appropriate PET-based normalization, the tracer uptake should define brain anatomy in sufficient details, which is not always the case for PET molecular imaging radiotracers. Finally, the spatial distribution of the tracer should be reasonably similar across subjects, to prevent bias in registration. This is not the case for amyloid tracers, where tracer distribution varies markedly across individuals, depending on the degree of amyloid burden: while in positive cases GM uptake is on par with WM uptake, amyloid-negative subjects display high contrast between the two.

Building on these premises, there is a need for validated methods to perform reliable spatial normalization of PET amyloid images. In this view, and considering that most PET clinical studies are nowadays performed using PET/Computed Tomography (CT) systems, we tested and validated a method for a high precision spatial normalization and

SUVr computation using the low-dose CT image acquired for attenuation correction (AC). The inclusion of a CT-based analytical pipeline for PET quantification would allow a net benefit in terms of both research and clinical practice, allowing the recruitment of larger samples and favoring clinical routine analysis.

2. Materials and methods

2.1. Participants

Subjects were retrieved from the Ricerca Finalizzata Progetto di Rete Nazionale AD (AD-NETWORK/RETEAD) database. RETEAD is a large Italian multicenter study that aims at developing and validating operational research criteria for diagnosis of AD in the preclinical/predemential phase and early recognition of atypical forms, based on a multi-factorial protocol that integrates molecular, imaging, neuropsychological and clinical profiles. The study conformed to the ethical standards of the Declaration of Helsinki for protection of human subjects. Each subject provided written informed consent as approved by the Local Ethical Committees.

Thirty four subjects (age = 69.58 ± 6.63 (range:50–80) years; M/F = 16/18) were recruited at Fondazione IRCCS Istituto Neurologico Besta, Milan. The sample consisted of subjects in preclinical and prodromal dementia phases and patients with overt dementia, thus covering a wide spectrum of cases, from normal cognition to dementia. In detail, the sample included 4 subjects with subjective cognitive complaints (Jessen et al., 2014), 12 subjects with pre-mild cognitive impairment (pre-MCI) (Storandt et al., 2006), 14 subjects with MCI (8 single-domain MCI and 6 multi-domain MCI) (McKhann et al., 2011b) and 4 patients with a diagnosis of probable AD dementia (McKhann et al., 2011a). Each subject underwent brain structural imaging, including an MRI scan at Fondazione IRCCS Istituto Neurologico Besta, Milan and an amyloid PET/CT scan at the Nuclear Medicine Unit of San Raffaele Hospital, Milan. Inter-scan interval was no longer than six months for MRI and amyloid PET scans.

2.2. Image acquisition

2.2.1. ^{18}F-Florbetaben PET/CT

Each subject received an intravenous injection of 300 ± − 37 MBq of ^{18}F-Florbetaben (Neuraceq, Piramal). The dose was administered as a single bolus injection followed by 20 cc of saline flush. All PET acquisition were performed using a hybrid PET/CT Discovery-690 system (General Electric Medical Systems Milwaukee, WI, USA) (Bettinardi et al., 2011). After positioning, a low dose CT scan (kVp: 140 kV, current: 40 mA, rotation time: 0.8 s, slice thickness: 3.75 mm, pitch: 1.375:1) was acquired to be used for attenuation correction of PET data. Images were reconstructed using the "standard" kernel, a 30 cm reconstruction field of view, and 3.27 mm slice interval, for a resulting voxel size of $0.59 \times 0.59 \times 3.27$ mm^3. A 3D-PET acquisition (list mode) was started about 90 min after the injection of the tracer and lasted for 20 min. Image reconstruction was performed by using a 3D Ordered Subsets Expectation Maximization (OSEM) algorithm with the following parameters: Image matrix = 128, Field Of View = 250 mm, Subsets = 24, Iterations = 3, Post Filter (Gaussian) = 3 mm FWHM, Attenuation Correction = CT-based. The resulting voxel size was $1.95 \times 1.95 \times 3.27$ mm^3.

2.2.2. MRI

The MRI imaging data were acquired in Neurological Institute "C. Besta", using an Achieva 3 T MR scanner (Philips Healthcare BV, Best, NL) equipped with a 32-channel head coil. A volumetric turbo field echo (TFE) T1-weighted structural sequence (180 sagittal slices, TR = 8.3 ms, TE = 3.9 ms, FOV = 240 × 240 mm, voxel size = 1x1x1 mm^3, flip angle = 8°) was acquired for each subject. Other structural, diffusion and functional magnetic imaging data were also

collected in the same session, but not reported in this study. The total duration of scanning session was around 55 min.

2.2.3. Image processing

All CT and MRI images were converted from the original DICOM to a NIFTI format using SPM12. The origin coordinates of the MRI scan were manually set to the anterior commissure. CT and PET images were rigidly co-registered to the respective MRI scan. A visual inspection was always performed as a quality control to detect possible errors in the co-registration step.

2.3. Spatial normalization

2.3.1. CT-based normalization algorithm

The hypothesis of the proposed procedure is that a low dose CT scan contains enough information in terms of contrast between GM, WM and cerebro-spinal fluid (CSF) to estimate the spatial transformation accurately. To spatially normalize the CT images into the stereotactic/standard space, we optimized the unified segmentation-normalization algorithm as implemented by Ashburner and Friston in SPM12 (Ashburner and Friston, 2005). This algorithm iteratively finds the spatial transformation that best matches the analyzed image to a set of tissue probability maps (TPM), that are used in a subsequent tissue classification procedure.

The algorithm works with a parametrization of the image intensities for each tissue type using a Gaussian Mixture Model (GMM). In the latest version, known as "new segment", included in SPM12 (Malone et al., 2015; Weiskopf et al., 2011), 6 tissue classes are considered: GM, WM, CSF, bone, outside tissues and air. A priori TPM are used to improve the segmentation, to fix initial intensities for each tissue class and to distinguish tissues with identical average intensities. This iterative algorithm first estimates the spatial deformation from the Montreal Neurological Institute (MNI) space to the subject native space. The TPM are then transformed to the subject native space using this deformation and they are used to update the GMM describing the intensities of all tissues. Finally, the spatial transformation from the MNI space to the native space is updated, looking for the one that best matches the current GMM. The procedure is iterated until the algorithm converges. Forward and backward transformations are both estimated.

In our proposed optimization, the CT images are pre-processed by a "clean-up" procedure. Every value lower than -300 HU is set to -1024 HU, to avoid low-density structures outside the head (e.g.: head-holder, cushion etc.) confounding the algorithm. Without this procedure, the coarse affine registration performed before the actual segmentation often fails. The resulting images are then loaded in the SPM12 unified segmentation algorithm, with optimized parameters. Compared to the default SPM12 settings for MRI, we disabled bias-field correction, as CT does not suffer from this artifact. Also, as Hounsfield values are generally comprised in a fixed and narrow range in CT, we used only 1 Gaussian for the GMM of GM, WM, and only 2 Gaussians for the other 4 classes (CSF, bone, outside tissue and air). Identical regularization strengths to the default were used. All the parameters used are summarized in Table 1. The number of Gaussians was chosen a priori, knowing that in CT GM and WM have only one average intensity. For CSF, 2 Gaussians were used to take into account the possibility that CSF close to the bone has higher intensity than that in the ventricles due to spillover effect. As bone has values in a very broad range in CT, 2 gaussians were used. Tissue can be thought as composed of low-intensity fat and higher-intensity areas like muscles, so 2 gaussians also were used. In the "air" class we expect all low intensity structures that have the same value of -1024, after our thresholding, modeled with 1 gaussian, and another Gaussian to model all the other low intensity pixels between about -50 to -300 HU.

The robustness of our algorithm to different settings was tested in supplementary material.

Table 1
Settings for the unified segmentation algorith.

Setting	Parameter	CT	MRI (default SPM settings)
Bias Field Correction	FWHM	Disabled	60 mm
	Regularization		Light
Tissue GMM: Number of Gaussians	GM	1	1
	WM	1	1
	CSF	2	2
	Bone	2	3
	Tissue	2	4
	Air	2	2
Warping regularization	Absolute displacement	0	0
	Membrane Energy	0.001	0.001
	Bending Energy	0.5	0.5
	Linear Elasticity 1	0.05	0.05
	Linear Elasticity 2	0.2	0.2

2.3.2. MRI-based spatial normalization

MRI images were spatially normalized to the MNI space using the SPM12 unified segmentation and default settings. The parameters are reported in Table 1, to be compared to the optimization introduced for the CT version. The segmented tissues and the forward transformation to the MNI space are then saved. The spatial transformation was used as a comparison with the CT one. The GM map was also used in a later stage to compare and validate the proposed method (see below).

2.4. Comparison of the CT and MRI normalizations

Two strategies were used to compare the output of the normalization procedures, with the MRI-based normalization considered as the gold standard for the pre-processing step. First, we measured, from the two normalized CT- ($nPET_{CT}$) and MRI-based ($nPET_{MRI}$) ^{18}F-Florbetaben PET images, the SUVr values in a set of ROIs commonly considered to estimate amyloid burden in AD. The second strategy consisted in measuring, for each subject, the degree of overlap between the two estimated GM maps (GM_{CT} and GM_{MRI}) obtained with the CT- and the MRI-derived transformations. Normalized ^{18}F-Florbetaben PET images were resampled to a bounding box of [-90–126 -72; 90 90,108] mm with an isotropic voxel size of 2 mm, using the two previously estimated deformations.

2.4.1. ^{18}F-Florbetaben SUVr estimation

Multiple ROIs for regional and global amyloid burden assessment were selected according to previous literature (Barthel et al., 2011; Ong et al., 2013; Sabri et al., 2015; Tiepolt et al., 2016) To summarize, we extracted six ROIs representing wide, bilateral cortical macroareas (Fig. 1), i.e. Dorsolateral and Medial Frontal Cortex, Cingulum, Precuneus, Inferior and Superior Parietal Lobules, Lateral Occipital Cortex, and Lateral Temporal Cortex, from the Automated Anatomical Labeling (AAL) atlas (Tzourio-Mazoyer et al., 2002), through the Wake Forest University PickAtlas toolbox for SPM (Maldjian et al., 2003). All the images were scaled to the activity of the cerebellar GM, used as the reference region (Catafau et al., 2016; Villemagne et al., 2015). The average computed from the six ROIs was considered as an index of global cortical amyloid burden.

2.4.2. Statistical analysis

Concordance between the SUVr measures was assessed using Bland-Altman plots and estimation of region-wise Pearson correlation analysis. Regional and global amyloid burdens and standard deviations were computed with mean absolute differences and limits of agreement (see Table 2).
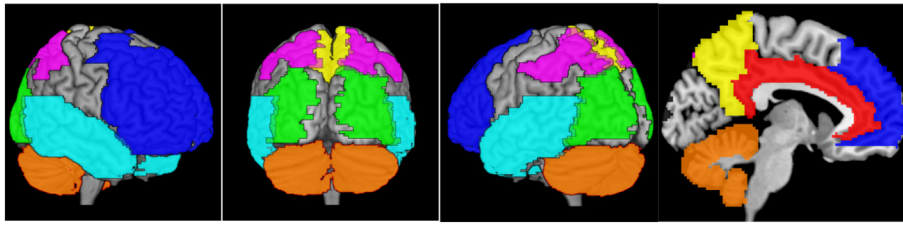
Fig. 1. Visualization of the regions of interest used for the analysis, overlaid on a standardized template.

Table 2
Regional and global amyloid SUVr.

ROI	CT-based	MRI-based	Absolute Difference	Limits of Agreement
Frontal cortex	1.25	1.28	0.030	− 0.125 | 0.066
Cingulum	1.39	1.44	0.044	− 0.110 | 0.022
Precuneus	1.39	1.42	0.026	− 0.099 | 0.047
Temporal cortex	1.34	1.35	0.010	− 0.079 | 0.056
Occipital cortex	1.44	1.40	0.048	− 0.067 | 0.160
Parietal cortex	1.25	1.26	0.011	− 0.087 | 0.064
Whole cortical regions	1.34	1.35	0.012	− 0.075 | 0.051

Regional SUVr computed on the whole brain considering the two different spatial normalization pipelines (see text). Values are shown as means, while limits of agreement are computed as: mean(d)-1.96*sd(d) | mean(d) + 1.96*sd (d).

2.4.3. Comparison of gray matter maps

The GM maps obtained from the MRI segmentation of each patient were resampled to the MNI space within a bounding box of [−90–126 -72; 90 90,108] with an isotropic voxel size of 1 mm, to better capture the limited thickness of GM. The MRI and the CT derived deformations were used to obtain a GM_{MRI} and a GM_{CT} map for each subject. It is reasonable to expect a complete overlap of the two maps in the case of identical deformations. Therefore, we measured the percentage of voxels in the GM_{CT} that overlap with those in the GM_{MRI}. The GM_{MRI} was then dilated to the 6 nearest-neighbor voxels in three dimensions, and this dilated map was used again as a reference to perform the same computation. This allowed the assessment of the fraction of GM that was transformed either to the correct location or to a 1 mm wide neighborhood. This dilation was performed two more times to measure concordance within 2 mm and 3 mm wide from the reference. These overlap measures were computed over the whole image and also locally, inside the same ROIs defined for the SUVr analysis.

3. Results

3.1. ^{18}F-Florbetaben SUVr

The main steps of the proposed procedure are shown in Fig. 2. The mean regional $SUVr_{CT}$ and $SUVr_{MRI}$ as well as the composite cortical values are reported in Table 2. Negligible differences were found at regional level. Occipital SUVr scores showed some deviation, but were still negligible (mean absolute difference 0.048, limits of agreement − 0.067 | 0.160), whereas the temporal SUVr scores showed the best concordance (mean absolute difference 0.010, limits of agreement − 0.079 | 0.056). When compared to the regional $SUVr_{MRI}$, the $SUVr_{CT}$ was slightly underestimated for all regions, except for the occipital region which showed the opposite trend. Global amyloid burden showed very narrow differences using average regional $SUVr_{CT}$ or $SUVr_{MRI}$ (mean ± sd 0.012 ± 0.032), as further confirmed by the Bland-Altman plot (Fig. 3) and correlation analysis (Pearson $r = 0.994$, $p < 2.2e-16$) (Fig. 3). In the Bland-Altman plot of the global SURr, we performed a Spearman correlation to test whether there was a trend between the $SUVr_{CT}$ vs $SUVr_{MRI}$ difference and the global SUVr load. There was a trend with $\rho^2 = 0.16$, which is significant with $p = .02$.

In supplementary materials we show that these results are affected by the exact algorithms settings, at least when using reasonable parameters.

3.2. Comparison of gray matter maps

The overlap between GM maps obtained using the two different transformations is shown in Fig. 4. Transforming the GM maps using the CT-based normalization algorithm provided a 70% overlap with those obtained with MR-based normalization. Notably, > 90% of the GM map voxels from the CT-based normalization were within 1 mm from the MR-transformed ones. Full results including 2 and 3 mm dilation are reported in Table 3.

4. Discussion

A correct AD diagnosis in early prodromal, and even preclinical, disease stages is important, especially for the appropriate inclusion of patients in clinical trials (Sperling et al., 2014a, 2014b). In this framework, amyloid-PET is unique for the detection of pathological Aβ accumulation in vivo (Vandenberghe et al., 2013a,b). Amyloid positivity, as shown by PET studies, is currently considered as a supportive biomarker for AD diagnosis according to the diagnostic criteria (Albert et al., 2011; Dubois et al., 2014; McKhann et al., 2011a; Sperling et al., 2011). Validated and standardized amyloid (semi)quantification procedures are therefore needed to overcome the limitations of visual ratings and/or binary classifications, for both diagnostic and research purposes (Perani et al., 2014b), and also for a better evaluation of cases for clinical trials. To this end, there is a need to develop highly reliable (semi)quantification approaches to accurately measure amyloid burden in different brain regions at the single-subject level. Previous studies have focused on how to optimize Amyloid-PET analysis to improve both quantification (Bullich et al., 2017a; Saint-Aubert et al., 2014) and reliability of longitudinal PET assessments (Brendel et al., 2015; Bullich et al., 2017b). Notably, semi-quantification with SUVr increased the classification accuracy in comparison to visual ratings (Bullich et al., 2017a; Camus et al., 2012; Perani et al., 2014b).

The majority of previous studies has focused on the development of highly accurate processing steps for the quantification, especially considering reference and target region selection and definition of optimal scanning protocols. The present study, however, focuses on the preprocessing phase, with the aim of validating a feasible CT-based pipeline which could greatly increase the implementation of semi-quantification protocols in research and clinical settings.

When performing PET data analysis in standard space, spatial normalization is the first and a crucial step for the accurate estimation of radioligand specific uptake. High-precision spatial alignment of brain structures is indeed fundamental to achieve the highest statistical power. High resolution MRI images are currently considered the gold standard for spatial warping and many algorithms are available to compute the individual spatial transformations. MRI scans require extra costs and time, on top of being a procedure that cannot be performed on all patients (e.g. in presence of metallic inserts, or due to claustrophobia). While these limitations might not be relevant in research settings, MRI scans are not always acquired in routine studies in clinical settings.
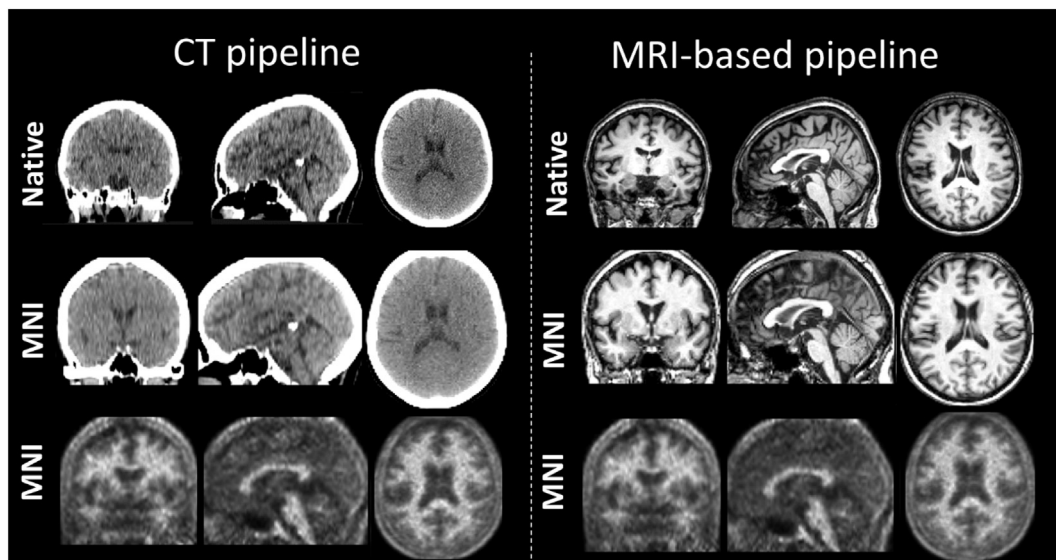
Fig. 2. Images of the normalization methods in a representative patient. Left: CT based normalization, Right: MRI based normalization. Top: Native Space structural images; Middle: normalized structural images; Bottom: Amyloid Images normalized with the respective pipelines. MNI: Montreal Neurological Institute.

The CT acquisition protocol resulted in a volumetric CT Dose Index (CTDI$_{vol}$) of about 1.5 mGy, which translated to a Dose Length Product (DLP) of about 25 mGy*cm, meaning, in an average patient, a dose of $< 70\,\mu$Sv. This dose provides sufficient anatomical details while being extremely low. In this work CT were acquired using 40 mA current and 0.8 s rotation time. The most recent scanners, like ours, can be set up to acquire images with currents as low as 10 mA and lower rotation times, for even lower doses. However, not only the image quality significantly decreases, but also there is the risk of "photon starvation" artefacts, which lead to incorrect attenuation correction (Xia et al., 2012). To overcome this limit, new methods are being used where the current is not lowered but the number of projections acquired is reduced, using then sparse view reconstruction techniques (Rui et al., 2015). However, these techniques have only been recently introduced clinically and they have not been optimized to provide anatomical detail.

A limit of this study is that the influence of CT image quality on the algorithm could not be studied. Future studies will need to assess both the lower dose limit at which the algorithm still performs correctly, and also whether the use of diagnostic quality CT provides improvements.

Here we found high concordance with MRI-based normalization using the CT-based normalization procedure. Notably, considering the SUVr values, the standard deviation of the differences between the reference MRI-based normalization and the proposed algorithm was <0.05 in all the considered ROIs. Therefore, this semi-quantitative approach allowed for an accurate measurement of the amyloid burden in each ROI, which is of importance since regional variations of amyloid burden are well-documented in literature (Jansen et al., 2015; Ossenkoppele et al., 2015). Additionally, in the second validation test, comparing the CT- and MRI-based GM maps registration, we found that the maps overlapped within 1 mm in 90% of the voxels. This validation was run on a patient population that spanned over a wide range of pathological stages and of amyloid burden, where brain anatomy might differ due to increased atrophy. Accordingly, global amyloid SUVr for our population ranged from 0.9 to 1.8 SUVr. A very small trend, $\rho^2 = 0.16$, was noted in the Bland-Altman plot. Considering that the *p*-value was at the threshold for statistical significance ($p = .02$), this result might be due to the presence of few outliers. Studying this algorithm on larger number of subjects, especially AD with high amyloid load and high levels of atrophy, could further certify the good
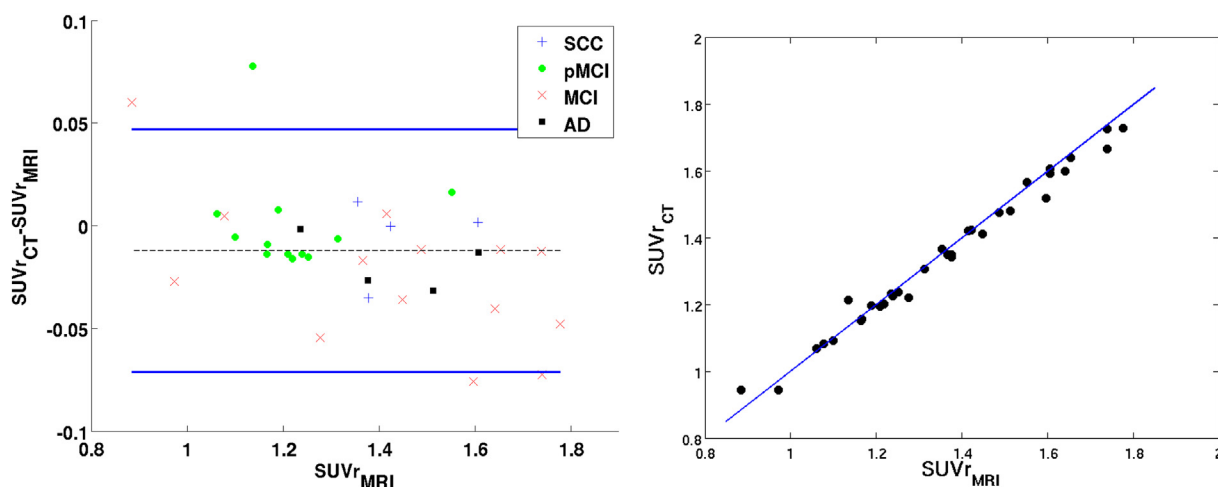
Fig. 3. Left: Bland-Altman Plot showing the agreement between the two normalization procedures when quantifying the whole cortical SUVr. Subjects are color coded by their initial diagnosis. Right: Scatter plot showing the correlation between whole cortical SUVr scores obtained using the two procedures. Blue diagonal line represents the identity (y = x) line.
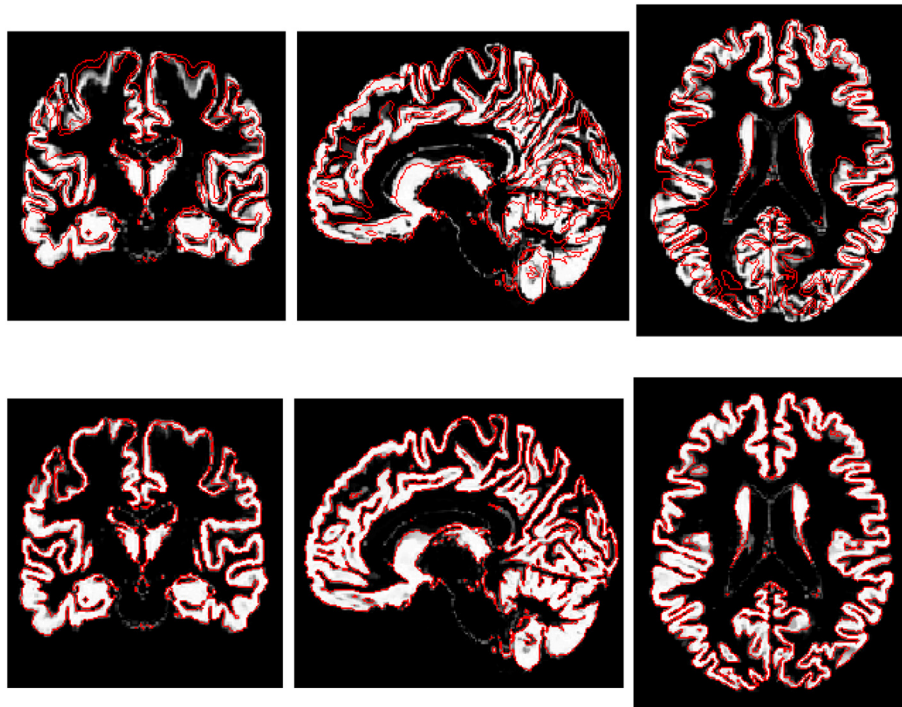
Fig. 4. Gray matter segmentation of a representative patient, transformed to the MNI space. Top: CT-based deformation, bottom: MR-based deformation. A contour was drawn on the bottom-row images and applied to the top row, to facilitate comparison.

Table 3
Gray matter maps overlap.

ROI	Search range			
	Voxel	1 mm	2 mm	3 mm
	[%]	[%]	[%]	[%]
Frontal cortex	66	88	96	98.7
Cingulum	76	93	98	99.6
Precuneus	68	90	97	99.1
Temporal cortex	73	92	98	99.6
Occipital cortex	66	90	97	99.1
Parietal cortex	59	85	95	98.1
Cerebellum	85	96	99	99.7
Whole cortical regions	70	90	97	98.9

Degree of overlap between GM maps normalized using CT-based method, and the reference ones (MRI-based) as a function of the distance needed for the overlap around the reference map (Voxel level, 1 mm, 2 mm, 3 mm).

performance of this algorithm in all the possible conditions. In Supplementary Materials, we have also shown that the algorithm is robust to changes in the settings, concerning to how the thresholding operation is performed and to the number of gaussians used for outside tissues.

The proposed CT normalization procedure was developed for hybrid PET/CT scanners, since this is the most widely diffuse system for both clinical and research applications. This approach does not require any tracer-specific template to determine the spatial normalization. Notably, while the present procedure was validated using the ^{18}F-Florbetaben tracer, it can be adopted as well with other radioligands. This CT-based approach could also be useful for analyzing large retrospective databases where CT, but not MRI, scans are only available. Another important application could be the development of an automated processing pipeline that can aid clinicians in the evaluation of amyloid PET scans. Finally, it should be noted that this procedure was built exclusively using widely available and validated free tools: SPM and the AAL atlas.

5. Conclusions

In this work, we validated an automated spatial normalization method for amyloid PET data, based on the low-dose CT acquired contextually with the PET scan for attenuation correction. This procedure, when compared to the gold-standard MRI-based spatial transformation, showed extremely high levels of concordance in the results of semi-quantification. The procedure is well-suited for both clinical and research applications as well as for radioligands other than amyloid-tracers since it has a simple implementation and is based on validated and widely available tools.

Conflict of interest

The authors declare that they have no conflicts of interest regarding the publication of this article.

Acknowledgments and funding

Declarations of interest

None.

Appendix A. Supplementary data

Supplementary data to this article can be found online at https://doi.org/10.1016/j.nicl.2018.07.013.

References

Ahmed, R.M., Paterson, R.W., Warren, J.D., Zetterberg, H., O'Brien, J.T., Fox, N.C., Halliday, G.M., Schott, J.M., 2014. Biomarkers in dementia: clinical utility and new directions. J. Neurol. Neurosurg. Psychiatry 85, 1426–1434. https://doi.org/10.1136/jnnp-2014-307662.

Albert, M.S., Dekosky, S.T., Dickson, D., Dubois, B., Feldman, H.H., Fox, N.C., Gamst, A., Holtzman, D.M., Jagust, W.J., Petersen, R.C., Snyder, P.J., Carrillo, M.C., Thies, B., Phelps, C.H., 2011. The diagnosis of mild cognitive impairment due to Alzheimer's disease: recommendations from the National Institute on Aging-Alzheimer's Association workgroups on diagnostic guidelines for Alzheimer's disease. Alzheimers Dement. 7, 270–279. https://doi.org/10.1016/j.jalz.2011.03.008.

Aleman-Gomez, Y., Melie-Garcia, L., Valdés-Hernandez, P., 2006. IBASPM: toolbox for automatic parcellation of brain structures. In: 12th Annual Meeting of the Organization for Human Brain Mapping, pp. 11–15.

Armstrong, M.J., Litvan, I., Lang, A.E., Bak, T.H., Bhatia, K.P., Borroni, B., Boxer, A.L., Dickson, D.W., Grossman, M., Hallett, M., Josephs, K.A., Kertesz, A., Lee, S.E., Miller, B.L., Reich, S.G., Riley, D.E., Tolosa, E., Tröster, A.I., Vidailhet, M., Weiner, W.J., 2013. Criteria for the diagnosis of corticobasal degeneration. Neurology 80, 496–503. https://doi.org/10.1212/WNL.0b013e31827f0fd1.

Ashburner, J., Friston, K.J., 2005. Unified segmentation. NeuroImage 26, 839–851. https://doi.org/10.1016/j.neuroimage.2005.02.018.

Barthel, H., Gertz, H.-J., Dresel, S., Peters, O., Bartenstein, P., Buerger, K., Hiemeyer, F., Wittemer-Rump, S.M., Seibyl, J., Reininger, C., Sabri, O., 2011. Cerebral amyloid-β PET with florbetaben (18F) in patients with Alzheimer's disease and healthy controls: a multicentre phase 2 diagnostic study. Lancet Neurol. 10, 424–435. https://doi.org/10.1016/S1474-4422(11)70077-1.

Bettinardi, V., Presotto, L., Rapisarda, E., Picchio, M., Gianolli, L., Gilardi, M.C., 2011. Physical performance of the new hybrid PET/CT Discovery-690. Med. Phys. 38, 5394–5411. https://doi.org/10.1118/1.3635220.

Brendel, M., Högenauer, M., Delker, A., Sauerbeck, J., Bartenstein, P., Seibyl, J., Rominger, A., 2015. Improved longitudinal [18F]-AV45 amyloid PET by white matter reference and VOI-based partial volume effect correction. NeuroImage 108, 450–459. https://doi.org/10.1016/j.neuroimage.2014.11.055.

Bullich, S., Seibyl, J., Catafau, A.M., Jovalekic, A., Koglin, N., Barthel, H., Sabri, O., De Santi, S., 2017a. Optimized classification of 18F-Florbetaben PET scans as positive and negative using an SUVR quantitative approach and comparison to visual assessment. NeuroImage. Clin. 15, 325–332. https://doi.org/10.1016/j.nicl.2017.04.025.

Bullich, S., Villemagne, V.L., Catafau, A.M., Jovalekic, A., Koglin, N., Rowe, C.C., De Santi, S., 2017b. Optimal reference region to measure longitudinal amyloid-β change with 18F-Florbetaben PET. J. Nucl. Med. 58, 1300–1306. https://doi.org/10.2967/jnumed.116.187351.

Camus, V., Payoux, P., Barré, L., Desgranges, B., Voisin, T., Tauber, C., La Joie, R., Tafani, M., Hommet, C., Chételat, G., Mondon, K., de La Sayette, V., Cottier, J.P., Beaufils, E., Ribeiro, M.J., Gissot, V., Vierron, E., Vercouillie, J., Vellas, B., Eustache, F., Guilloteau, D., 2012. Using PET with 18F-AV-45 (florbetapir) to quantify brain amyloid load in a clinical environment. Eur. J. Nucl. Med. Mol. Imaging 39, 621–631. https://doi.org/10.1007/s00259-011-2021-8.

Catafau, A.M., Bullich, S., Seibyl, J.P., Barthel, H., Ghetti, B., Leverenz, J., Ironside, J.W., Schulz-Schaeffer, W.J., Hoffmann, A., Sabri, O., 2016. Cerebellar amyloid-β plaques: how frequent are they, and do they influence 18F-Florbetaben SUV ratios? J. Nucl. Med. 57, 1740–1745. https://doi.org/10.2967/jnumed.115.171652.

Chiotis, K., Carter, S.F., Farid, K., Savitcheva, I., Nordberg, A., 2015. Amyloid PET in European and North American cohorts; and exploring age as a limit to clinical use of amyloid imaging. Eur. J. Nucl. Med. Mol. Imaging 42, 1492–1506. https://doi.org/10.1007/s00259-015-3115-5.

Clark, C.M., Pontecorvo, M.J., Beach, T.G., Bedell, B.J., Coleman, R.E., Doraiswamy, P.M., Fleisher, A.S., Reiman, E.M., Sabbagh, M.N., Sadowsky, C.H., Schneider, J.A., Arora, A., Carpenter, A.P., Flitter, M.L., Joshi, A.D., Krautkramer, M.J., Lu, M., Mintun, M.A., Skovronsky, D.M., 2012. Cerebral PET with florbetapir compared with neuropathology at autopsy for detection of neuritic amyloid-β plaques: a prospective cohort study. Lancet Neurol. 11, 669–678. https://doi.org/10.1016/S1474-4422(12)70142-4.

Dubois, B., Feldman, H.H., Jacova, C., Hampel, H., Molinuevo, J.L., Blennow, K., Dekosky, S.T., Gauthier, S., Selkoe, D., Bateman, R., Cappa, S., Crutch, S., Engelborghs, S., Frisoni, G.B., Fox, N.C., Galasko, D., Habert, M.O., Jicha, G.A., Nordberg, A., Pasquier, F., Rabinovici, G., Robert, P., Rowe, C., Salloway, S., Sarazin, M., Epelbaum, S., de Souza, L.C., Vellas, B., Visser, P.J., Schneider, L., Stern, Y., Scheltens, P., Cummings, J.L., 2014. Advancing research diagnostic criteria for Alzheimer's disease: the IWG-2 criteria. Lancet Neurol. 13, 614–629. https://doi.org/10.1016/S1474-4422(14)70090-0.

Fleisher, A.S., 2011. Using positron emission tomography and Florbetapir F 18 to image cortical amyloid in patients with mild cognitive impairment or dementia due to Alzheimer disease. Arch. Neurol. 68, 1404. https://doi.org/10.1001/archneurol.2011.150.

Hutton, C., Declerck, J., Mintun, M.A., Pontecorvo, M.J., Devous, M.D., Joshi, A.D., 2015. Quantification of 18F-florbetapir PET: comparison of two analysis methods. Eur. J. Nucl. Med. Mol. Imaging 42, 725–732. https://doi.org/10.1007/s00259-015-2988-7.

Iaccarino, L., Sala, A., Caminiti, S.P., Perani, D., 2017. The emerging role of PET imaging in dementia. F1000Research 6, 1830. https://doi.org/10.12688/f1000research.11603.1.

Jansen, W.J., Ossenkoppele, R., Knol, D.L., Tijms, B.M., Scheltens, P., Verhey, F.R.J., Visser, P.J., Aalten, P., Aarsland, D., Alcolea, D., Alexander, M., Almdahl, I.S., Arnold, S.E., Baldeiras, I., Barthel, H., van Berckel, B.N.M., Bibeau, K., Blennow, K., Brooks, D.J., van Buchem, M.A., Camus, V., Cavedo, E., Chen, K., Chetelat, G., Cohen, A.D., Drzezga, A., Engelborghs, S., Fagan, A.M., Fladby, T., Fleisher, A.S., van der Flier, W.M., Ford, L., Förster, S., Fortea, J., Foskett, N., Frederiksen, K.S., Freund-Levi, Y., Frisoni, G.B., Froelich, L., Gabryelewicz, T., Gill, K.D., Gkatzima, O., Gómez-Tortosa, E., Gordon, M.F., Grimmer, T., Hampel, H., Hausner, L., Hellwig, S., Herukka, S.-K., Hildebrandt, H., Ishihara, L., Ivanoiu, A., Jagust, W.J., Johannsen, P., Kandimalla, R., Kapaki, E., Klimkowicz-Mrowiec, A., Klunk, W.E., Köhler, S., Koglin, N., Kornhuber, J., Kramberger, M.G., Van Laere, K., Landau, S.M., Lee, D.Y., de Leon, M., Lisetti, V., Lleó, A., Madsen, K., Maier, W., Marcusson, J., Mattsson, N., de Mendonça, A., Meulenbroek, O., Meyer, P.T., Mintun, M.A., Mok, V., Molinuevo, J.L., Møllergård, H.M., Morris, J.C., Mroczko, B., Van der Mussele, S., Na, D.L., Newberg, A., Nordberg, A., Nordlund, A., Novak, G.P., Paraskevas, G.P., Parnetti, L., Perera, G., Peters, O., Popp, J., Prabhakar, S., Rabinovici, G.D., Ramakers, I.H.G.B., Rami, L., Resende De Oliveira, C., Rinne, J.O., Rodrigue, K.M., Rodríguez-Rodríguez, E., Roe, C.M., Rot, U., Rowe, C.C., Rüther, E., Sabri, O., Sanchez-Juan, P., Santana, I., Sarazin, M., Schröder, J., Schütte, C., Seo, S.W., Soetewey, F., Soininen, H., Spiru, L., Struyfs, H., Teunissen, C.E., Tsolaki, M., Vandenberghe, R., Verbeek, M.M., Villemagne, V.L., Vos, S.J.B., van Waalwijk van Doorn, L.J.C., Waldemar, G., Wallin, A., Wallin, Å.K., Wiltfang, J., Wolk, D.A., Zboch, M., Zetterberg, H., 2015. Prevalence of cerebral amyloid pathology in persons without dementia. JAMA 313, 1924. https://doi.org/10.1001/jama.2015.4668.

Jessen, F., Amariglio, R.E., van Boxtel, M., Breteler, M., Ceccaldi, M., Chételat, G., Dubois, B., Dufouil, C., Ellis, K.A., van der Flier, W.M., Glodzik, L., van Harten, A.C., de Leon, M.J., McHugh, P., Mielke, M.M., Molinuevo, J.L., Mosconi, L., Osorio, R.S., Perrotin, A., Petersen, R.C., Rabin, L.A., Rami, L., Reisberg, B., Rentz, D.M., Sachdev, P.S., de la Sayette, V., Saykin, A.J., Scheltens, P., Shulman, M.B., Slavin, M.J., Sperling, R.A., Stewart, R., Uspenskaya, O., Vellas, B., Visser, P.J., Wagner, M., 2014. A conceptual framework for research on subjective cognitive decline in preclinical Alzheimer's disease. Alzheimers Dement. 10, 844–852. https://doi.org/10.1016/j.jalz.2014.01.001.

Lancaster, J.L., Rainey, L.H., Summerlin, J.L., Freitas, C.S., Fox, P.T., Evans, A.C., Toga, A.W., Mazziotta, J.C., 1997. Automated labeling of the human brain: a preliminary report on the development and evaluation of a forward-transform method. Hum. Brain Mapp. 5, 238–242. https://doi.org/10.1002/(SICI)1097-0193(1997)5:4<238::AID-HBM6>3.0.CO;2-4.

Lancaster, J.L., Woldorff, M.G., Parsons, L.M., Liotti, M., Freitas, C.S., Rainey, L., Kochunov, P.V., Nickerson, D., Mikiten, S.A., Fox, P.T., 2000. Automated Talairach atlas labels for functional brain mapping. Hum. Brain Mapp. 10, 120–131. https://doi.org/10.1002/1097-0193(200007)10:3<120::AID-HBM30>3.0.CO;2-8.

Lundqvist, R., Lilja, J., Thomas, B.A., Lotjonen, J., Villemagne, V.L., Rowe, C.C., Thurfjell, L., 2013. Implementation and validation of an adaptive template registration method for 18F-Flutemetamol imaging data. J. Nucl. Med. 54, 1472–1478. https://doi.org/10.2967/jnumed.112.115006.

Maldjian, J.A., Laurienti, P.J., Kraft, R.A., Burdette, J.H., 2003. An automated method for neuroanatomic and cytoarchitectonic atlas-based interrogation of fMRI data sets. NeuroImage 19, 1233–1239. https://doi.org/10.1016/S1053-8119(03)00169-1.

Malone, I.B., Leung, K.K., Clegg, S., Barnes, J., Whitwell, J.L., Ashburner, J., Fox, N.C., Ridgway, G.R., 2015. Accurate automatic estimation of total intracranial volume: a nuisance variable with less nuisance. NeuroImage 104, 366–372. https://doi.org/10.1016/j.neuroimage.2014.09.034.

McKeith, I.G., Boeve, B.F., Dickson, D.W., Halliday, G., Taylor, J.-P., Weintraub, D., Aarsland, D., Galvin, J., Attems, J., Ballard, C.G., Bayston, A., Beach, T.G., Blanc, F., Bohnen, N., Bonanni, L., Bras, J., Brundin, P., Burn, D., Chen-Plotkin, A., Duda, J.E., El-Agnaf, O., Feldman, H., Ferman, T.J., Ffytche, D., Fujishiro, H., Galasko, D., Goldman, J.G., Gomperts, S.N., Graff-Radford, N.R., Honig, L.S., Iranzo, A., Kantarci, K., Kaufer, D., Kukull, W., Lee, V.M.Y., Leverenz, J.B., Lewis, S., Lippa, C., Lunde, A., Masellis, M., Masliah, E., McLean, P., Mollenhauer, B., Montine, T.J., Moreno, E., Mori, E., Murray, M., O'Brien, J.T., Orimo, S., Postuma, R.B., Ramaswamy, S., Ross, O.A., Salmon, D.P., Singleton, A., Taylor, A., Thomas, A., Tiraboschi, P., Toledo, J.B., Trojanowski, J.Q., Tsuang, D., Walker, Z., Yamada, M., Kosaka, K., 2017. Diagnosis and management of dementia with Lewy bodies. Neurology 89, 88–100. https://doi.org/10.1212/WNL.0000000000004058.

McKhann, G.M., Knopman, D.S., Chertkow, H., Hyman, B.T., Jack, C.R., Kawas, C.H., Klunk, W.E., Koroshetz, W.J., Manly, J.J., Mayeux, R., Mohs, R.C., Morris, J.C., Rossor, M.N., Scheltens, P., Carrillo, M.C., Thies, B., Weintraub, S., Phelps, C.H., 2011a. The diagnosis of dementia due to Alzheimer's disease: recommendations from the National Institute on Aging-Alzheimer's Association workgroups on diagnostic guidelines for Alzheimer's disease. Alzheimers Dement. 7, 263–269. https://doi.org/10.1016/j.jalz.2011.03.005.

McKhann, G.M., Knopman, D.S., Chertkow, H., Hyman, B.T., Jack, C.R., Kawas, C.H., Klunk, W.E., Koroshetz, W.J., Manly, J.J., Mayeux, R., Mohs, R.C., Morris, J.C., Rossor, M.N., Scheltens, P., Carrillo, M.C., Thies, B., Weintraub, S., Phelps, C.H., Albert, M.S., Dekosky, S.T., Dickson, D., Dubois, B., Feldman, H.H., Fox, N.C., Gamst, A., Holtzman, D.M., Jagust, W.J., Petersen, R.C., Snyder, P.J., Carrillo, M.C., Thies, B., Phelps, C.H., 2011b. The diagnosis of mild cognitive impairment due to Alzheimer's disease: recommendations from the National Institute on Aging-Alzheimer's Association workgroups on diagnostic guidelines for Alzheimer's disease. Alzheimers Dement. 7, 270–279. https://doi.org/10.1016/j.jalz.2011.03.005.

Nordberg, A., Carter, S.F., Rinne, J., Drzezga, A., Brooks, D.J., Vandenberghe, R., Perani, D., Forsberg, A., Långström, B., Scheinin, N., Karrasch, M., Någren, K., Grimmer, T., Miederer, I., Edison, P., Okello, A., Van Laere, K., Nelissen, N., Vandenbulcke, M., Garibotto, V., Almkvist, O., Kalbe, E., Hinz, R., Herholz, K., 2013. A European multicentre PET study of fibrillar amyloid in Alzheimer's disease. Eur. J. Nucl. Med. Mol. Imaging 40, 104–114. https://doi.org/10.1007/s00259-012-2237-2.

Oh, H., Steffener, J., Razlighi, Q.R., Habeck, C., Liu, D., Gazes, Y., Janicki, S., Stern, Y., 2015. Aβ-related hyperactivation in frontoparietal control regions in cognitively normal elderly. Neurobiol. Aging 36, 3247–3254. https://doi.org/10.1016/j.neurobiolaging.2015.08.016.

Ong, K., Villemagne, V.L., Bahar-Fuchs, A., Lamb, F., Chételat, G., Raniga, P., Mulligan, R.S., Salvado, O., Putz, B., Roth, K., Masters, C.L., Reininger, C.B., Rowe, C.C., 2013. 18F-florbetaben Aβ imaging in mild cognitive impairment. Alzheimers Res. Ther. 5, 4. https://doi.org/10.1186/alzrt158.

Ong, K.T., Villemagne, V.L., Bahar-Fuchs, A., Lamb, F., Langdon, N., Catafau, A.M.,

Stephens, A.W., Seibyl, J., Dinkelborg, L.M., Reininger, C.B., Putz, B., Rohde, B., Masters, C.L., Rowe, C.C., 2015. Aβ imaging with 18F-florbetaben in prodromal Alzheimer's disease: a prospective outcome study. J. Neurol. Neurosurg. Psychiatry 86, 431–436. https://doi.org/10.1136/jnnp-2014-308094.

Ossenkoppele, R., Jansen, W.J., Rabinovici, G.D., Knol, D.L., van der Flier, W.M., van Berckel, B.N.M., Scheltens, P., Visser, P.J., Verfaillie, S.C.J., Zwan, M.D., Adriaanse, S.M., Lammertsma, A.A., Barkhof, F., Jagust, W.J., Miller, B.L., Rosen, H.J., Landau, S.M., Villemagne, V.L., Rowe, C.C., Lee, D.Y., Na, D.L., Seo, S.W., Sarazin, M., Roe, C.M., Sabri, O., Barthel, H., Koglin, N., Hodges, J., Leyton, C.E., Vandenberghe, R., van Laere, K., Drzezga, A., Forster, S., Grimmer, T., Sánchez-Juan, P., Carril, J.M., Mok, V., Camus, V., Klunk, W.E., Cohen, A.D., Meyer, P.T., Hellwig, S., Newberg, A., Frederiksen, K.S., Fleisher, A.S., Mintun, M.A., Wolk, D.A., Nordberg, A., Rinne, J.O., Chételat, G., Lleo, A., Blesa, R., Fortea, J., Madsen, K., Rodrigue, K.M., Brooks, D.J., 2015. Prevalence of amyloid PET positivity in dementia syndromes. JAMA 313, 1939. https://doi.org/10.1001/jama.2015.4669.

Perani, D., Iaccarino, L., Bettinardi, V., 2014a. The need for "objective measurements" in FDG and amyloid PET neuroimaging. Clin. Transl. Imaging 2, 331–342. https://doi.org/10.1007/s40336-014-0072-0.

Perani, D., Schillaci, O., Padovani, A., Nobili, F.M., Iaccarino, L., Della Rosa, P.A., Frisoni, G., Caltagirone, C., 2014b. Erratum to "A Survey of FDG- and Amyloid-PET Imaging in Dementia and GRADE Analysis". Biomed. Res. Int. 2014, 1. https://doi.org/10.1155/2014/246586.

Rascovsky, K., Hodges, J.R., Knopman, D., Mendez, M.F., Kramer, J.H., Neuhaus, J., van Swieten, J.C., Seelaar, H., Dopper, E.G.P., Onyike, C.U., Hillis, A.E., Josephs, K.A., Boeve, B.F., Kertesz, A., Seeley, W.W., Rankin, K.P., Johnson, J.K., Gorno-Tempini, M.-L.M.L., Rosen, H., Prioleau-Latham, C.E., Lee, A., Kipps, C.M., Lillo, P., Piguet, O., Rohrer, J.D., Rossor, M.N., Warren, J.D., Fox, N.C., Galasko, D., Salmon, D.P., Black, S.E., Mesulam, M., Weintraub, S., Dickerson, B.C., Diehl-Schmid, J., Pasquier, F., Deramecourt, V., Lebert, F., Pijnenburg, Y., Chow, T.W., Manes, F., Grafman, J., Cappa, S.F., Freedman, M., Grossman, M., Miller, B.L., 2011. Sensitivity of revised diagnostic criteria for the behavioural variant of frontotemporal dementia. Brain 134, 2456–2477. https://doi.org/10.1093/brain/awr179.

Rowe, C.C., Villemagne, V.L., 2013. Brain amyloid imaging. J. Nucl. Med. Technol. 41, 11–18. https://doi.org/10.2967/jnumed.110.076315.

Rui, X., Cheng, L., Long, Y., Fu, L., Alessio, A.M., Asma, E., Kinahan, P.E., De Man, B., 2015. Ultra-low dose CT attenuation correction for PET/CT: analysis of sparse view data acquisition and reconstruction algorithms. Phys. Med. Biol. 60, 7437–7460. https://doi.org/10.1088/0031-9155/60/19/7437.

Sabri, O., Sabbagh, M.N., Seibyl, J., Barthel, H., Akatsu, H., Ouchi, Y., Senda, K., Murayama, S., Ishii, K., Takao, M., Beach, T.G., Rowe, C.C., Leverenz, J.B., Ghetti, B., Ironside, J.W., Catafau, A.M., Stephens, A.W., Mueller, A., Koglin, N., Hoffmann, A., Roth, K., Reininger, C., Schulz-Schaeffer, W.J., 2015. Florbetaben PET imaging to detect amyloid beta plaques in Alzheimer's disease: phase 3 study. Alzheimers Dement. 11, 964–974. https://doi.org/10.1016/j.jalz.2015.02.004.

Saint-Aubert, L., Nemmi, F., Péran, P., Barbeau, E.J., Payoux, P., Chollet, F., Pariente, J., 2014. Comparison between PET template-based method and MRI-based method for cortical quantification of florbetapir (AV-45) uptake in vivo. Eur. J. Nucl. Med. Mol. Imaging 41, 836–843. https://doi.org/10.1007/s00259-013-2656-8.

Salloway, S., Sperling, R., Fox, N.C., Blennow, K., Klunk, W., Raskind, M., Sabbagh, M., Honig, L.S., Porsteinsson, A.P., Ferris, S., Reichert, M., Ketter, N., Nejadnik, B., Guenzler, V., Miloslavsky, M., Wang, D., Lu, Y., Lull, J., Tudor, I.C., Liu, E., Grundman, M., Yuen, E., Black, R., Brashear, H.R., 2014. Two phase 3 trials of Bapineuzumab in mild-to-moderate Alzheimer's disease. N. Engl. J. Med. 370, 322–333. https://doi.org/10.1056/NEJMoa1304839.

Schmidt, M.E., Chiao, P., Klein, G., Matthews, D., Thurfjell, L., Cole, P.E., Margolin, R., Landau, S., Foster, N.L., Mason, N.S., De Santi, S., Suhy, J., Koeppe, R.A., Jagust, W., 2015. The influence of biological and technical factors on quantitative analysis of amyloid PET: points to consider and recommendations for controlling variability in longitudinal data. Alzheimers Dement. 11, 1050–1068. https://doi.org/10.1016/j.jalz.2014.09.004.

Sevigny, J., Chiao, P., Bussière, T., Weinreb, P.H., Williams, L., Maier, M., Dunstan, R., Salloway, S., Chen, T., Ling, Y., O'Gorman, J., Qian, F., Arastu, M., Li, M., Chollate, S., Brennan, M.S., Quintero-Monzon, O., Scannevin, R.H., Arnold, H.M., Engber, T., Rhodes, K., Ferrero, J., Hang, Y., Mikulskis, A., Grimm, J., Hock, C., Nitsch, R.M., Sandrock, A., 2016. The antibody aducanumab reduces Aβ plaques in Alzheimer's disease. Nature 537, 50–56. https://doi.org/10.1038/nature19323.

Sperling, R.A., Aisen, P.S., Beckett, L.A., Bennett, D.A., Craft, S., Fagan, A.M., Iwatsubo, T., Jack, C.R., Kaye, J., Montine, T.J., Park, D.C., Reiman, E.M., Rowe, C.C., Siemers, E., Stern, Y., Yaffe, K., Carrillo, M.C., Thies, B., Morrison-Bogorad, M., Wagster, M.V., Phelps, C.H., 2011. Toward defining the preclinical stages of Alzheimer's disease: recommendations from the National Institute on Aging-Alzheimer's Association workgroups on diagnostic guidelines for Alzheimer's disease. Alzheimers Dement. 7, 280–292. https://doi.org/10.1016/j.jalz.2011.03.003.

Sperling, R., Mormino, E., Johnson, K., 2014a. The evolution of preclinical Alzheimer's disease: implications for prevention trials. Neuron 84, 608–622. https://doi.org/10.1016/j.neuron.2014.10.038.

Sperling, R.A., Rentz, D.M., Johnson, K.A., Karlawish, J., Donohue, M., Salmon, D.P., Aisen, P., 2014b. The A4 study: stopping AD before symptoms begin? Sci. Transl. Med. 6, 228fs13. https://doi.org/10.1126/scitranslmed.3007941.

Storandt, M., Grant, E.A., Miller, J.P., Morris, J.C., 2006. Longitudinal course and neuropathologic outcomes in original vs revised MCI and in pre-MCI. Neurology 67, 467–473. https://doi.org/10.1212/01.wnl.0000228231.26111.6e.

Tiepolt, S., Hesse, S., Patt, M., Luthardt, J., Schroeter, M.L., Hoffmann, K.-T., Weise, D., Gertz, H.-J., Sabri, O., Barthel, H., 2016. Early [18F]florbetaben and [11C]PiB PET images are a surrogate biomarker of neuronal injury in Alzheimer's disease. Eur. J. Nucl. Med. Mol. Imaging 43, 1700–1709. https://doi.org/10.1007/s00259-016-3353-1.

Tzourio-Mazoyer, N., Landeau, B., Papathanassiou, D., Crivello, F., Etard, O., Delcroix, N., Mazoyer, B., Joliot, M., 2002. Automated anatomical labeling of activations in SPM using a macroscopic anatomical Parcellation of the MNI MRI single-subject brain. NeuroImage 15, 273–289. https://doi.org/10.1006/nimg.2001.0978.

Vandenberghe, R., Van Laere, K., Ivanoiu, A., Salmon, E., Bastin, C., Triau, E., Hasselbalch, S., Law, I., Andersen, A., Korner, A., Minthon, L., Garraux, G., Nelissen, N., Bormans, G., Buckley, C., Owenius, R., Thurfjell, L., Farrar, G., Brooks, D.J., 2010. 18 F-flutemetamol amyloid imaging in Alzheimer disease and mild cognitive impairment: a phase 2 trial. Ann. Neurol. 68, 319–329. https://doi.org/10.1002/ana.22068.

Vandenberghe, R., Adamczuk, K., Dupont, P., Van Laere, K., Chételat, G., 2013a. Amyloid PET in clinical practice: its place in the multidimensional space of Alzheimer's disease. NeuroImage Clin. 2, 497–511. https://doi.org/10.1016/j.nicl.2013.03.014.

Vandenberghe, R., Adamczuk, K., Van Laere, K., 2013b. The interest of amyloid PET imaging in the diagnosis of Alzheimer's disease. Curr. Opin. Neurol. 26, 646–655. https://doi.org/10.1097/WCO.0000000000000036.

Villemagne, V.L., 2016. Amyloid imaging: past, present and future perspectives. Ageing Res. Rev. 30, 95–106. https://doi.org/10.1016/j.arr.2016.01.005.

Villemagne, V.L., Bourgeat, P., Doré, V., Macaulay, L., Williams, R., Ames, D., Martins, R.N., Salvado, O., Chen, K., Reiman, E.M., Masters, C.L., Rowe, C.C., 2015. Amyloid imaging in therapeutic trials: the quest for the optimal reference region. Alzheimers Dement. 11, P21–P22. https://doi.org/10.1016/j.jalz.2015.06.036.

Weiskopf, N., Lutti, A., Helms, G., Novak, M., Ashburner, J., Hutton, C., 2011. Unified segmentation based correction of R1 brain maps for RF transmit field inhomogeneities (UNICORT). NeuroImage 54, 2116–2124. https://doi.org/10.1016/j.neuroimage.2010.10.023.

Wolk, D.A., 2011. Association between in vivo fluorine 18–labeled Flutemetamol amyloid positron emission tomography imaging and in vivo cerebral cortical histopathology. Arch. Neurol. 68, 1398. https://doi.org/10.1001/archneurol.2011.153.

Xia, T., Alessio, A.M., De Man, B., Manjeshwar, R., Asma, E., Kinahan, P.E., 2012. Ultra-low dose CT attenuation correction for PET/CT. Phys. Med. Biol. 57, 309–328. https://doi.org/10.1088/0031-9155/57/2/309.